

DIFFERENTIAL ROTATION IN MAGNETIZED AND NON-MAGNETIZED STARS

JUN MABUCHI¹, YOUHEI MASADA¹ AND AKIRA KAGEYAMA¹

Submitted to ApJ, Preprint typeset using L^AT_EXstyle

ABSTRACT

Effects of magnetic field on stellar differential rotation are studied by comparing magnetohydrodynamic (MHD) models and their hydrodynamic (HD) counterparts in the broad range of rotation rate and in varying initial rotation profile. Fully-compressible MHD simulations of rotating penetrative convection are performed in a full-spherical shell geometry. Critical conditions for the transition of the differential rotation between faster equator (solar-type) and slower equator (anti-solar type) are explored with focusing on the “Rossby number (Ro)” and the “convective Rossby number (Ro_{conv})”. It is confirmed that the transition is more gradual and the critical value for it is higher in the MHD model than the HD model in the view of the Ro_{conv} -dependence. The rotation profile shows, as observed in earlier studies, the bistability near the transition in the HD model, while it disappears when allowing the growth of magnetic fields except for the model with taking anti-solar type solution as the initial condition. We find that the transition occurs at $Ro \simeq 1$ both in the MHD and HD models independently of the hysteresis. Not only the critical value, the sharpness of the transition is also similar between the two models in the view of the Ro -dependence. The influences of the dynamo-generated magnetic field and/or the hysteresis on convective motion are reflected in the Ro . This would be the reason why the transition is unified in the view of the Ro -dependence. We finally discuss the Ro -dependence of magnetic dynamo activities with emphasis on its possible relation to the kinetic helicity profile.

Subject headings: convection–magnetohydrodynamics (MHD) – Sun: interior – Stars: rotation

1. INTRODUCTION

The differential rotation (DR) is believed to be a key ingredient in organizing large-scale magnetic fields in the solar interior. Most of standard solar dynamo scenarios rely heavily on, so-called Ω -effect as the amplification process of magnetic fields to reproduce observed solar magnetic activity with cyclic polarity reversals and butterfly-shaped spatiotemporal migrations (see, e.g., Charbonneau 2005, 2010, for reviews). However, we have not yet arrived at a full understanding of the physical mechanism for maintaining the solar differential rotation. See, e.g., Miesch (2005) for a review.

The internal rotation profile of the Sun has been uncovered by the global helioseismology (e.g., Kosovichev et al. 1997; Thompson et al. 2003; Howe 2009). A striking feature of the solar rotation profile is its equatorial acceleration: The plasma near the equator rotates faster than other parts in the convection zone. While the bulk of the convection zone is characterized by conical iso-rotation contours, the strong radial shear is concentrated in the near-surface layer and the tachocline underlying the convection zone (e.g., Schou et al. 1998; Charbonneau et al. 1999; Basu & Antia 2001). The equatorward angular momentum transport due to the turbulent Reynolds stress induced by the rotating stratified convection is mainly responsible for the solar-type DR with equatorial acceleration (e.g., Krause & Rüdiger 1974; Ruediger 1989; Kitchatinov & Rüdiger 1995; Miesch 2005).

The possibility of the opposite profile, or anti-solar type DR, in which the equatorial region is rotating slower, has been suggested numerically since the early 3D hydrodynamic simulation of rotating spherical-shell convection by Gilman (1977) over a broad range of parameters and various simulation setups (see Glatzmaier & Gilman 1982; Brun & Toomre 2002; Aurnou et al. 2007; Steffen & Freytag 2007; Chan

2010; Käpylä et al. 2011; Gastine et al. 2013). However, although the solar-type DR has been frequently observed in various types and ages of the stars, the anti-solar type DR has only been reported for a few of K giant stars observed with the Doppler imaging technique (Strassmeier et al. 2003; Weber et al. 2005; Kovári et al. 2007, 2014). It is still unclear how common the anti-solar type DR is in the solar-like main-sequence dwarfs and what really separates the two rotation regimes.

Bearing in mind these situations, the transition between the solar and anti-solar type rotation profiles has been extensively studied by the simulation of spherical shell convection in recent years. Käpylä et al. (2011) found in fully-compressible convection simulation that the transition is characterized by the Coriolis number (inverse of the Rossby number which is defined in §2) and is only weakly dependent on the density stratification. Guerrero et al. (2013) explored the physics of large-scale flows in solar-like stars by using an anelastic large-eddy simulation with stratification resembling the solar interior. They confirmed that the two regimes of the DR exist even in the solar-like strongly stratified internal structure. The critical Rossby number they obtained was consistent with that in Käpylä et al. (2011).

The systematic parameter study of the transition between the solar and anti-solar type rotation profiles was conducted by Gastine et al. (2014) with rotating spherical shell simulations of anelastic and Boussinesq convections (see also Gastine et al. 2013). They found, by combining their massive simulation results with the models of the different research groups, that the transition is controlled by the “convective Rossby number”, almost independently of the model setup, such as thickness of the convective envelope and density stratification. In addition, they found that two kinds of DR profiles are two possible bistable states around the transition, suggesting the hysteresis of the stellar rotation profile. The bistability of the rotation profile, discovered by Gastine et al. (2014), was confirmed independently by Käpylä et al. (2014) in hydrody-

¹ Department of Computational Science, Graduate School of System Informatics, Kobe University; Kobe 657-8501, contact: ymasada@harbor.kobe-u.ac.jp

dynamic simulations of the compressible convection. However, the influence of magnetic field on the rotation profile and its transition is still controversial despite the magnetic field is an inevitable outcome of electrically-conducting fluid motions (e.g., Moffatt 1978; Krause & Raedler 1980).

In Masada et al. (2013) (hereafter MYK13), we suggested, for the first time, that the formation of the solar-type DR is associated with the development of the magnetic field : It was found that the anti-solar type DR profile at the early dynamo kinematic stage transits to the solar-type profile after the dynamo-generated magnetic field beginning to affect the convective motion (see §4.1 in MYK13). Such a magnetic influence on the rotation profile was confirmed by independent groups recently. Fan & Fang (2014) performed anelastic convective dynamo simulation of the model with the realistic solar internal structure, solar rotation rate and solar luminosity. They showed that the dynamo-generated magnetic field plays a crucial role in attaining the solar rotation profile in the actual solar parameter regime, i.e., the rotation profile becomes the anti-solar type without the magnetic field. They also reported that the bistability of the rotation profile, discovered in earlier studies, disappears when allowing the evolution of the magnetic field. The facilitation of the solar-type DR and the disappearance of the bistability of the rotation profile due to the magnetic field were confirmed by Karak et al. (2014), in which they studied the effect of the magnetic field on the rotation profiles around the transition by fully-compressible convective dynamo simulations.

In this paper, we systematically study the effect of the magnetic field on rotating spherical shell convection and resultant mean DR by comparing the MHD models with their hydrodynamics counterparts (HD models) in the broad range of the initial rotation rate. The bistable nature of the rotation profile is revisited under the influence of the magnetic field. A self-consistent, fully-compressible Yin-Yang MHD code which was developed in MYK13 and a stellar model consisting of the convection zone and the radiative zone are used for the simulation. The primary objective of this paper is to explore a key parameter which controls the transition between the anti-solar type and solar-type DR profiles and its dependence on the magnetic field and the initial rotation profile (§3.1–3.3). We cast a spotlight on two diagnostic parameters, i.e., the ‘‘Rossby number’’ and the ‘‘convective Rossby number’’ (see §2 for the definitions). The magnetic dynamo activity in the MHD models with the different rotation rates is also studied in §3.4. After discussing the relation between the magnetic dynamo activity and the convection properties in §4, we summarize our findings in §5.

2. SIMULATION SETUP

The simulation setup is almost the same as the model A of MYK13. We numerically solve a MHD convection system in a spherical shell domain defined by $(0.6R \leq r \leq R)$, $(0 \leq \theta \leq \pi)$, and $(-\pi \leq \phi < \pi)$, where r , θ , and ϕ are radius, colatitude, and longitude, respectively. Our model consists of two-layers, which qualitatively resemble the solar interior: stably stratified layer of thickness $0.1R$ in the range $(0.6R \leq r \leq 0.7R)$ and surrounding convective envelope of thickness $0.3R$ in $(0.7R \leq r \leq R)$.

The basic equations are the fully-compressible MHD equations in the rotating frame with a constant angular velocity $\Omega = \Omega_0 e_z$ which is parallel to the coordinate axis ($\theta = 0$):

$$\frac{\partial \rho}{\partial t} = -\nabla \cdot f, \quad (1)$$

$$\begin{aligned} \frac{\partial f}{\partial t} = & -\nabla \cdot (vf) - \nabla p + j \times B \\ & + \rho g + 2\rho v \times \Omega + \nu \left[\nabla^2 v + \frac{1}{3} \nabla (\nabla \cdot v) \right], \end{aligned} \quad (2)$$

$$\begin{aligned} \frac{\partial p}{\partial t} = & -v \cdot \nabla p - \gamma p \nabla \cdot v \\ & + (\gamma - 1) [\nabla \cdot (\kappa \nabla T) + \eta j^2 + \Phi], \end{aligned} \quad (3)$$

$$\frac{\partial A}{\partial t} = v \times B - \eta j, \quad (4)$$

with

$$\begin{aligned} \Phi = & 2\nu \left[e_{ij} e_{ij} - \frac{1}{3} (\nabla \cdot v)^2 \right], e_{ij} = \frac{1}{2} \left(\frac{\partial v_i}{\partial x_j} + \frac{\partial v_j}{\partial x_i} \right), \\ g = & -g_0 / r^2 e_r, B = \nabla \times A, j = \nabla \times B. \end{aligned}$$

Here the mass density ρ , pressure p , mass flux $f = \rho v$, magnetic field’s vector potential A are the basic variables. g_0 is the gravitational acceleration, assumed to be constant. We assume an ideal gas law $p = (\gamma - 1)\rho \epsilon_i$ with $\gamma = 5/3$, where ϵ_i is the internal energy. The viscosity, electrical resistivity, and thermal conductivity are represented by ν , η , and κ respectively.

The initial condition is a hydrostatic equilibrium which is described by a polytropic temperature distribution with the polytropic index m

$$\frac{dT}{dr} = \frac{-g_0 / r^2}{c_v (\gamma - 1)(m + 1)}, \quad (5)$$

where c_v is the specific heat at constant volume. We choose $m = 1$ and 3 for the upper convective envelope and the lower stable layer, respectively. The thermal conductivity κ is determined by requiring a constant luminosity, L , defined by $L \equiv -4\pi \kappa r^2 dT/dr$, throughout the domain.

Non-dimensional quantities are defined by setting $R = g_0 = \rho_0 = \mu_0 = 1$ where ρ_0 is the initial density at $r = 0.6R$. The units of length, time, velocity, density, and magnetic field are R , $\sqrt{R/g_0}$, $\sqrt{g_0 R}$, ρ_0 and $\sqrt{g_0 R \mu_0 \rho_0}$, respectively. The definitions of the Prandtl, magnetic Prandtl, and Rayleigh numbers are

$$\text{Pr} = \frac{\nu}{\chi}, \quad \text{Pm} = \frac{\nu}{\eta}, \quad \text{Ra} = \frac{g_0 d^4}{\nu \chi R^2} \left(-\frac{1}{c_p} \frac{ds}{dr} \right)_{r_m}, \quad (6)$$

where $\chi \equiv \kappa_m / (c_p \rho_m)$ is the thermal diffusivity measured at the middle of the convection zone ($r = r_m$), and $d = 0.3R$ is the thickness of the convective envelope. The stratification is controlled by a normalized pressure scale height at the surface $\xi_0 \equiv c_v (\gamma - 1) T_s / (g_0 / R)$, where T_s is the temperature at $r = R$. Here we use in all the models $\xi_0 = 0.3$, yielding a small density contrast between top and bottom boundaries about 3 (see Figure 1 in MYK13). This is a major difference between our model and actual Sun.

In this paper, we focus on the two physical non-dimensional quantities, one is the ‘‘Rossby number’’ (ratio of inertia to Coriolis forces) and the other is the ‘‘convective Rossby number’’ (ratio of buoyancy to Coriolis forces) (e.g., Gilman 1977; Gastine et al. 2014) which are given by

$$\text{Ro} = \text{Co}^{-1} = \frac{v_{\text{rms}} k_l}{2\Omega_0}, \quad \text{Ro}_{\text{conv}} = \left(\frac{\text{Ra}}{\text{PrTa}} \right)^{1/2}, \quad (7)$$

respectively, where $k_l = 2\pi/d$ is the wavenumber of the largest

TABLE 1

SUMMARY OF THE SIMULATION RUNS. THE LABELS OF MHD MODELS CONTAIN THE LETTER M. HD MODELS HAVE A LABEL BEGINNING WITH H. THE SECOND LETTER DENOTES THE INITIAL ROTATION PROFILE. THE LABELS OF BASIC RUNS WITH THE INITIAL RIGID ROTATION CONTAINS THE LETTER R. MODELS STARTED WITH A SOLAR-TYPE OR AN ANTI-SOLAR TYPE DR HAVE A LETTER S OR A. THE NUMBER INDICATES THE GIVEN ROTATION RATE Ω_0 WITH THE DECIMAL POINT REMOVED. THE MEAN QUANTITIES v_{rms} , B_{eq} , Ro , τ_c , ϵ_M , AND ϵ_K ARE EVALUATED AT THE SATURATED STATE IN THE CONVECTIVE ENVELOPE. THE SUPER-CRITICALITY LEVEL δ IS DEFINED BY $(Ra - Ra_c)/Ra_c$, WHERE $Ra_c \simeq 9.83E^{-1.16}$ WITH THE EKMAN NUMBER OF $E \equiv \nu/(\Omega_0 d_0^2)$. HERE WE ADOPT, AS THE CRITICAL RAYLEIGH NUMBER, THE FITTING FORMULA DERIVED BY AL-SHAMALI ET AL. (2004), IN WHICH THEY OBTAINED IT FROM THE SIMULATION OF THE SPHERICAL SHELL CONVECTION WITH VARYING THE SHELL THICKNESS AND THE EKMAN NUMBER. $\alpha_e = \bar{v}_\phi(r=R, \theta = \pi/2)/(\Omega_0 R)$ IS THE DR PARAMETER. IN THE FINAL COLUMN, THE RESULTANT DR PROFILES, S (SOLAR-TYPE) OR AS (ANTI-SOLAR TYPE), ARE SUMMARIZED.

	Ω_0	δ	v_{rms}	B_{eq}	τ_c	ϵ_K	ϵ_M	Ro	Ro_{conv}	α_e	type
MR00625	0.0625	155	0.037	0.028	8.0	1.3×10^{-3}	2.7×10^{-4}	6.272	3.737	-0.351	AS
MR0125	0.125	69	0.040	0.028	7.6	1.6×10^{-3}	4.0×10^{-4}	3.310	1.868	-0.386	AS
MR025	0.25	30	0.029	0.021	10.2	8.4×10^{-4}	8.8×10^{-4}	1.230	0.934	-0.094	AS
MR030	0.30	24	0.028	0.021	10.5	8.3×10^{-4}	7.4×10^{-4}	0.995	0.778	-0.069	AS
MR035	0.35	20	0.030	0.022	10.0	8.6×10^{-4}	2.6×10^{-4}	0.898	0.667	0.045	S
MR040	0.40	17	0.029	0.021	10.3	8.3×10^{-4}	2.4×10^{-4}	0.763	0.584	0.086	S
MR050	0.50	13	0.028	0.020	10.8	8.0×10^{-4}	2.5×10^{-4}	0.580	0.467	0.088	S
MR060	0.60	10	0.027	0.020	11.3	7.4×10^{-4}	2.7×10^{-4}	0.463	0.389	0.078	S
MR150	1.50	3	0.018	0.012	17.0	2.8×10^{-4}	2.9×10^{-4}	0.123	0.156	0.011	S
MR300	3.00	0.75	0.010	0.007	29.3	9.1×10^{-5}	4.4×10^{-4}	0.036	0.078	0.0003	S
HR00625	0.0625	155	0.040	0.029	7.4	1.5×10^{-3}	-	6.761	3.737	-0.257	AS
HR025	0.25	30	0.055	0.040	5.4	4.0×10^{-3}	-	2.306	0.934	-0.384	AS
HR030	0.30	24	0.056	0.040	5.4	4.5×10^{-3}	-	1.955	0.778	-0.371	AS
HR035	0.35	20	0.056	0.040	5.3	4.9×10^{-3}	-	1.683	0.667	-0.310	AS
HR040	0.40	17	0.057	0.040	5.3	5.2×10^{-3}	-	1.481	0.584	-0.296	AS
HR045	0.45	15	0.034	0.024	8.8	1.4×10^{-3}	-	0.796	0.519	0.105	S
HR050	0.50	13	0.034	0.024	8.9	1.4×10^{-3}	-	0.707	0.467	0.114	S
HR055	0.55	12	0.034	0.024	8.8	1.5×10^{-3}	-	0.649	0.425	0.135	S
HR060	0.60	10	0.034	0.024	8.8	1.6×10^{-3}	-	0.593	0.389	0.132	S
HR300	3.00	0.75	0.011	0.009	28.3	2.2×10^{-4}	-	0.037	0.078	0.010	S
MS025	0.25	30	0.030	0.021	10.0	8.4×10^{-4}	9.2×10^{-4}	1.254	0.934	-0.071	AS
MS030	0.30	24	0.030	0.021	10.2	7.7×10^{-4}	8.5×10^{-4}	1.031	0.778	-0.050	AS
MS035	0.35	20	0.030	0.022	10.0	8.3×10^{-3}	2.9×10^{-4}	0.896	0.667	0.065	S
HS030	0.30	24	0.053	0.042	5.7	4.8×10^{-3}	-	1.837	0.778	-0.370	AS
HS035	0.35	20	0.049	0.042	6.1	5.0×10^{-3}	-	1.462	0.667	-0.306	AS
HS040	0.40	17	0.035	0.026	8.5	1.4×10^{-3}	-	0.928	0.584	0.102	S
MA030	0.30	24	0.030	0.021	10.1	7.7×10^{-4}	7.6×10^{-4}	1.034	0.778	-0.062	AS
MA035	0.35	20	0.030	0.022	9.9	9.3×10^{-4}	4.0×10^{-4}	0.909	0.667	-0.017	AS
MA040	0.40	17	0.030	0.021	10.1	7.8×10^{-4}	2.7×10^{-4}	0.780	0.584	0.059	S
HA040	0.40	17	0.056	0.040	5.4	5.3×10^{-3}	-	1.459	0.584	-0.293	AS
HA045	0.45	15	0.055	0.040	5.4	5.3×10^{-3}	-	1.286	0.519	-0.281	AS
HA050	0.50	13	0.046	0.024	6.5	1.4×10^{-3}	-	0.974	0.467	0.111	S

convective eddies (this can be justified because of our weakly stratified system), $v_{\text{rms}} \equiv [(3/2)(v_\theta^2 + v_r^2)]^{1/2}$ is the mean velocity, and $\text{Ta} \equiv (2\Omega_0 d^2/\nu)^2$ is the Taylor number. Angular brackets denote time- and volume-average “in the convective envelope” at the saturated state. The definitions of v_{rms} and Co are almost identical to those in Käpylä et al. (2011, 2014) and Karak et al. (2014). Note that, in this study, the convective Rossby number is only a function of the rotation rate, i.e., $\text{Ro}_{\text{conv}} \propto \Omega_0^{-1}$, because the other parameters are fixed in our simulations (see following paragraphs).

The stress-free boundary condition for the velocity is imposed on both the radial boundaries. As for the magnetic field, we assume the perfect conductor at the inner boundary and the radial field condition at the outer boundary. A constant energy flux which drives the convective motion is imposed at the inner boundary and the temperature is fixed to be T_s at the outer boundary.

The equations (1)–(4) are solved by the second-order central difference scheme with spatial discretization with Yin-Yang grid. See Kageyama & Sato (2004) and MYK13 for details. Non-dimensional parameters $\text{Pr} = 0.27$, $\text{Pm} = 4.0$,

and $\text{Ra} = 2.2 \times 10^5$ (i.e., $\nu = 7.8 \times 10^{-5}$, $\eta = 2.0 \times 10^{-5}$, and $\kappa = 3.9 \times 10^{-4}$) are commonly adopted in all the models studied here. The total grid size for all the simulation runs is 81 (in r) \times 131 (in θ) \times 393 (in ϕ) \times 2 (Yin & Yang). To explore the response of the large-scale flow to the rotation rate, we vary the magnitude of Ω_0 in the MHD and HD models while keeping the background hydrostatic state unchanged. A random temperature perturbation and small “seed” magnetic field (only for MHD models) are introduced at the same time in the convection zone when the calculation starts.

3. NUMERICAL RESULTS

Our simulation models are summarized in Table 1. Model names are given in the left most column. The first letter in the model name denotes the presence and absence of the magnetic field. The labels of MHD models contain the letter M. HD models have a label beginning with H. The second letter denotes the initial rotation profile. The labels of basic runs with the initial rigid rotation contains the letter R. Models started with a solar-type or an anti-solar type DR have a letter S or A. The number indicates the given rotation rate Ω_0 with the

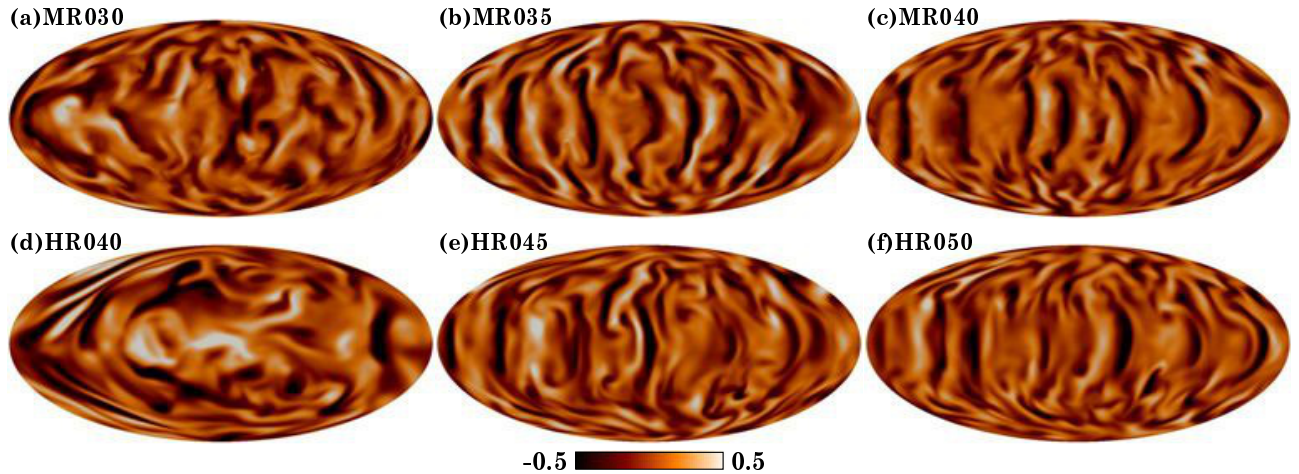


FIG. 1. — The radial velocity profile $v_r(r, \theta)$ at $r = 0.85R$ when $t \simeq 360\tau_c$ on a spherical surface. The normalization unit is the mean velocity v_{rms} of each model. The panels (a)–(c) correspond to the MHD models with $\Omega_0 = 0.3, 0.35$ and 0.4 , and the panels (d)–(f) are for the HD models with $\Omega_0 = 0.4, 0.45$ and 0.5 . The lighter and darker tones depict upflow and downflow velocities.

decimal point removed.

The mean quantities evaluated at the saturated state (v_{rms} , B_{eq} , τ_c , ϵ_K , and ϵ_M), the Rossby number (Ro), and the convective Rossby number (Ro_{conv}) are shown in Table 1, where $\tau_c \equiv d/v_{\text{rms}}$ is the convective turn-over time, $B_{\text{eq}} \equiv \langle (3/2)\rho(v_\theta^2 + v_r^2) \rangle^{1/2}$ is the equipartition strength of magnetic field, $\epsilon_K \equiv \langle \rho v^2 \rangle_{\text{fs}}/2$ and $\epsilon_M \equiv \langle B^2 \rangle_{\text{fs}}/2$ are the mean kinetic and magnetic energy densities. Angular brackets with subscript “fs” denote time- and volume-average in the full-spherical shell domain at the saturated state. As a measure of the convection strength, the estimated super-criticality level, defined by $\delta = (\text{Ra} - \text{Ra}_c)/\text{Ra}_c$, is shown in the second column, where Ra_c is the critical Rayleigh number (see caption for the definition of Ra_c). In the second last and last columns, DR parameter α_e (see §3.2 for the definition) and, the resultant DR profile, S (solar-type) or AS (anti-solar type), are summarized.

We perform three sets of runs. In the first set, we run models from the rigid rotation (Set R: Runs MR and HR) with the initial conditions described in §2. In the second and third sets, we examine the bistability of the rotation profile by taking either a solar-type (Set S: Runs MS and HS) and an anti-solar type (Set A: Runs MA and HA) solution as initial conditions. The MHD effects on the convective flows are studied in each set.

3.1. Convective Flows in Basic Runs with Initial Rigid Rotation

After the convective motion sets in, it reaches a saturated state before $\simeq 100\tau_c$ in the basic run with the initial rigid rotation. We have run the simulations up to around $400\tau_c$, which is almost comparable to the magnetic diffusion time, and studied the properties of the convective flow at the equilibrated state.

Figure 1 shows, in the Mollweide projection, the radial velocity distribution when $t \simeq 360\tau_c$ on spherical surface at $r = 0.85R$. The normalization unit is the mean velocity, v_{rms} , of each model. Panels (a)–(c) correspond to the MHD models (MR030, MR040, and MR045) and panels (d)–(f) are for the HD models (HR040, HR045, and HR050). The lighter and darker tones depict upflow and downflow velocities in the range $|v_r/v_{\text{rms}}| \leq 0.5$.

The rotating stratified convection is characterized by up-down asymmetry in all the models: the slower upflow dominant cells surrounded by the faster and narrower downflow lanes (e.g., Spruit et al. 1990; Miesch 2005). As the rotation rate increases, the convective cell shrinks and its structure is changed from the cellular pattern to the elongated columnar pattern formed in the equatorial region (e.g., Busse 1970; Glatzmaier & Gilman 1981; Brummell et al. 1996, 1998; Miesch et al. 2000). The transition from the cellular to columnar convections has been observed in earlier simulations (Käpylä et al. 2011, 2014; Gastine et al. 2013, 2014; Guerrero et al. 2013) and occurs at around $\Omega_0 = 0.35$ ($\text{Ro}_{\text{conv}} = 0.67$) in the MHD model but $\Omega_0 = 0.45$ ($\text{Ro}_{\text{conv}} = 0.52$) in the HD model. The magnetic field affects the convective motion, suggesting its impacts on the turbulent angular momentum transport and thus the resultant large-scale DR.

Shown in Figure 2 is the profile of the mean DR, defined by $\bar{\Omega}(r, \theta) = \bar{v}_\phi/(r \sin \theta) + \Omega_0$, where the overbar denotes the time- and azimuthal-average. The normalization unit is Ω_0 of each model. The time average spans in the range of $200 \lesssim t/\tau_c \lesssim 300$. Panels (a)–(c) correspond to the MHD models and panels (d)–(f) are the HD models. The red (blue) tone denotes the higher (lower) angular velocity. The white lines are iso-rotation contours. The interface between the convective envelope and the radiative layer is denoted by black dashed line.

As shown in earlier studies, there exists two regimes in the rotation profile: an anti-solar type DR with slower equator [(a) & (d)] and a solar-type DR with faster equator [(b),(c),(e) & (f)] (e.g., Gilman 1977; Käpylä et al. 2011, 2014; Gastine et al. 2013, 2014; Guerrero et al. 2013). While the anti-solar type DR is established in the model with the smaller rotation rate, the solar-type DR develops in the regime of the higher rotation rate. The most remarkable difference between the MHD and HD models is the critical rotation rate (and thus the critical convective Rossby number) for the transition. While the transition between the anti-solar and solar-type DR profiles occurs at around $\Omega_0 = 0.35$ ($\text{Ro}_{\text{conv}} = 0.67$) in the MHD model, it does at around $\Omega_0 = 0.45$ ($\text{Ro}_{\text{conv}} = 0.52$) in the HD model.

The DR profile is dominated by so-called “Taylor-Proudman balance” both in the MHD and HD models (e.g.,

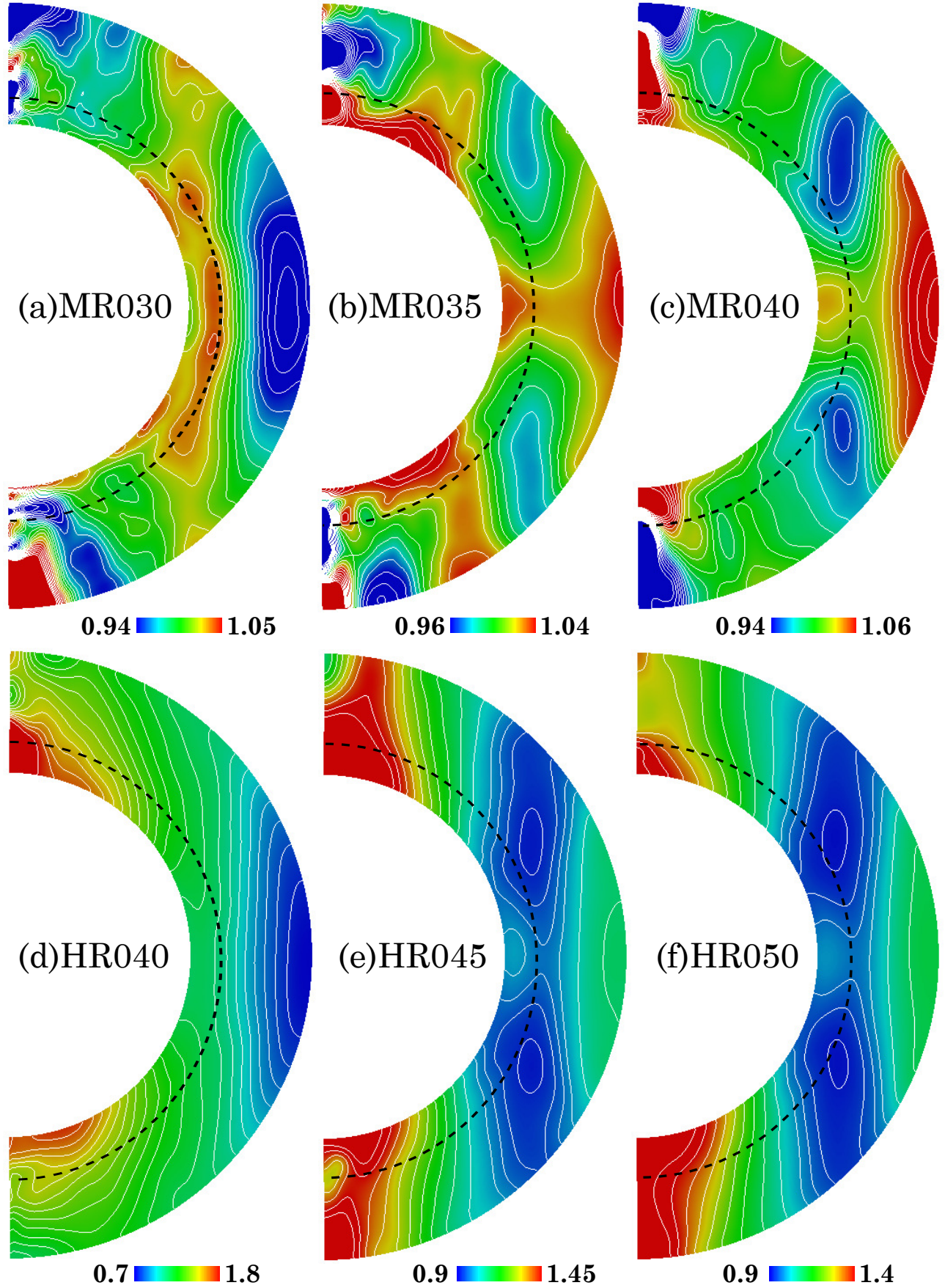


FIG. 2.— Time-averaged mean angular velocity $\bar{\Omega}(r, \theta)$. The panels (a)–(c) correspond to the MHD models with $\Omega_0 = 0.3, 0.35$ and 0.4 , and the panels (d)–(f) are for the HD models with $\Omega_0 = 0.4, 0.45$ and 0.5 . The white solid line denotes the iso-rotation contour. The black dashed line denotes the interface between convective and radiative zones.

Pedlosky 1987) and is still far from the solar conical isotachs deduced from the helioseismic measurement (e.g., Kitchatinov & Rüdiger 1995; Miesch 2005; Rempel 2005; Masada 2011). Nevertheless, it is intriguing that the iso-rotation contour is more conical in the MHD model than in the HD model. Especially, the radial shape of the isotachs is pronounced around the equator in the MHD model near the transition (see MR035).

When comparing the two models at the same rotation rate, we can see that the rotational shear is generally weaker in the MHD model. A strong polar jet (polar vortex) appeared in the HD model is also suppressed in the MHD model (see HR045 and HR050). In addition, the MHD effect seems to suppress the (viscous) spreading of the rotation profile of the convective envelope into the radiative layer in all the MHD models, as was observed in §4 of MYK13 (see, e.g., Spiegel & Zahn 1992; Gough & McIntyre 1998). The reduction of the rotational shear by the influence of the magnetic fields agrees with that has been reported in the earlier studies (e.g., Brun et al. 2004; Beaudoin et al. 2013; Fan & Fang 2014; Karak et al. 2014) and is discussed further in §3.2.

Figure 3 shows the time-averaged mean meridional flows. Panels (a)–(c) correspond to the MHD models and panels (d)–(f) are the HD models around the transition between the solar and anti-solar type rotation profiles. The color contour depicts the meridional flow velocity, defined by $v_m = (\bar{v}_r^2 + \bar{v}_\theta^2)^{1/2}$. The normalization unit is v_{rms} of each model. The streamlines are over-plotted with a length proportional to the flow speed. The white dashed line denotes the interface between the convective and radiative layers.

The circulation flow is primarily counter-clockwise (clockwise) in the bulk of the convection zone in the northern (southern) hemisphere. This is consistent with the observations of the solar sub-surface meridional flow (e.g., Komm et al. 1993; Giles et al. 1997; Ulrich 2010; Zhao et al. 2013), and a common feature of all the models. However, there is a difference in the circulation pattern. While a large single-cell is formed in the model with the anti-solar type DR (see MR030 and HR040), the model with the solar-type DR shows a multiple-cell pattern (see MR040 and HR050). A similar transition from single to multiple cell patterns of the meridional flow has been observed before in different settings (e.g., Käpylä et al. 2011, 2014; Gastine et al. 2013; Karak et al. 2014). We note that, as well as the rotation pattern, the transition of the meridional flow pattern occurs at lower Ω_0 (thus higher Ro_{conv}) in the MHD model than in the HD model.

3.2. Control Parameter of Differential Rotation

The transition between the anti-solar and solar-type DRs is a result of the structural difference of the whole three-dimensional convective motion separated at the critical rotation rate. Here we quantitatively examine the dependences of the DR profiles on two key diagnostic parameters, the convective Rossby number Ro_{conv} and the Rossby number Ro . Then we address which can better capture the transition between the anti-solar type and solar-type DRs. Following Gastine et al. (2014), we quantify the DR by the amplitude of the mean azimuthal flow at the equatorial surface:

$$\alpha_e = \frac{\bar{v}_\phi(r=R, \theta=\pi/2)}{\Omega_0 R}. \quad (8)$$

The positive and negative α_e denote the solar-type and anti-solar type DRs.

Figure 4(a) shows the DR parameter (α_e) as functions of the convective Rossby number (Ro_{conv}) [bottom axis] and the corresponding rotation rate (Ω_0) [top axis]. The blue crosses and red diamonds denote the MHD and HD models. The horizontal and vertical dashed lines indicate $\alpha_e = 0$ and $\text{Ro}_{\text{conv}} = 1$. As stated in § 3.1, the DR profile transits from the solar to anti-solar type regimes as the convective Rossby number increases. The absolute amplitude of α_e is, on average, larger in the anti-solar type DR than in the solar-type DR, and takes the maximum and minimum around the transition. These are common features of the two models and are compatible with earlier studies (Gastine et al. 2014; Käpylä et al. 2014; Karak et al. 2014). The critical value of Ro_{conv} for the transition is different in the two models. It occurs when $0.67 < \text{Ro}_{\text{conv}} < 0.78$ for the MHD model and $0.52 < \text{Ro}_{\text{conv}} < 0.58$ for the HD model, indicating a more gradual transition under the influence of the magnetic field. When comparing two models at the same Ro_{conv} , the magnitude of α_e is smaller in the MHD model than in the HD model. We confirm that the magnetic field has a role in suppressing the DR and helps to produce solar-type DR, which have been suggested in MYK13, Fan & Fang (2014) and Karak et al. (2014).

Our intriguing finding is that the critical value of the Rossby number for the transition is almost the same between the MHD and HD models. Shown in Figure 4(b) is the dependence of the DR parameter on the Rossby number (Ro). The blue crosses and red diamonds are corresponding to the MHD and HD models. The horizontal and vertical dashed lines denote $\alpha_e = 0$ and $\text{Ro} = 1$. The DR parameter decreases with the increase of the Rossby number in both models around the transition. The transition between the solar and anti-solar type DR profiles occurs at $\text{Ro} \simeq 1.0$ both in the MHD and HD models. Not only the critical value, the sharpness of the transition is also similar between the two models. The critical Rossby number for the transition obtained here gives a good agreement with that obtained in the hydrodynamic simulations by Käpylä et al. (2011, 2014). These indicate that the transition between the two rotation regimes is controlled by the Rossby number rather than by the convective Rossby number (i.e., the rotation rate itself in our study) regardless of the presence of the magnetic field.

We stress here that Karak et al. (2014) also studied the magnetic influence on the DR profile by comparing HD and MHD models, but did not discuss their Ro -dependences. Reading the critical Rossby number for the transition from Table 1 of Karak et al. (2014) and Käpylä et al. (2014), it is found that the transition occurs at a similar value of Ro in their MHD and HD models as well. Our finding is thus consistent with the earlier studies. The influence of the magnetic field on the DR profiles was also briefly mentioned in Gastine et al. (2014). However, they focused on the dependence of the DR profile on the “local Rossby number (Ro_l)” and did not examine its Ro -dependence. Here the local Rossby number is defined by $\text{Ro}_l = l_u \delta u_{\text{rms}} / (\pi \Omega_0 d)$, where δu_{rms} is the RMS value of the non-axisymmetric (fluctuating) component of the velocity (including both meridional and azimuthal components) and l_u is the mean spherical harmonic degree obtained from the kinetic energy spectrum (e.g., Christensen & Aubert 2006; Schirmer et al. 2012). Since they showed that the critical “local” Rossby number for the transition is different between MHD and HD models, we can say that the Rossby number is even better than the local Rossby number at least to describe the transition between the anti-solar and solar-type DR profiles in a unified manner.

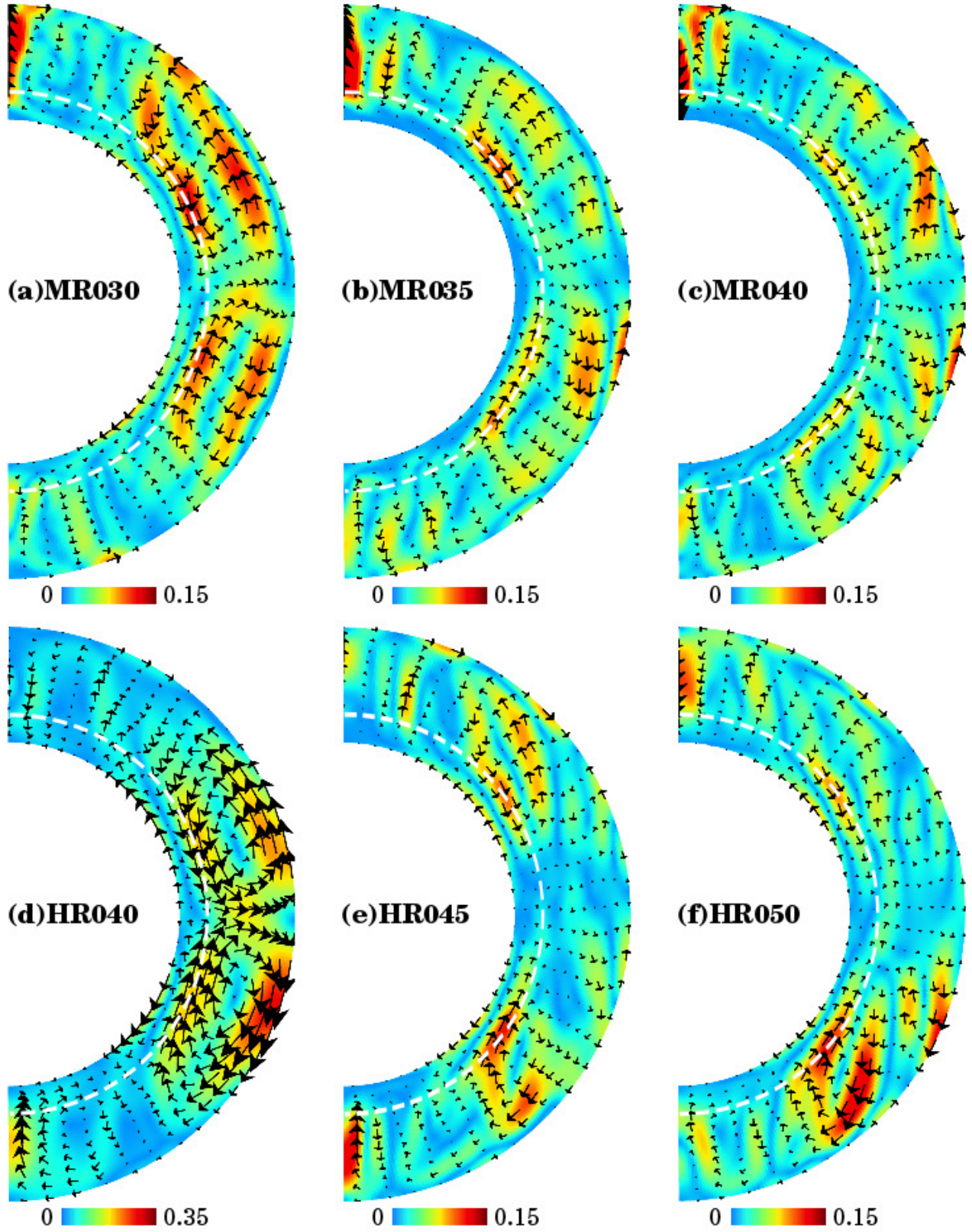


FIG. 3.— Time-averaged mean meridional flows. Panels (a)–(c) correspond to the MHD models (MR030, MR035, MR040) and panels (d)–(f) are the HD models (HR040, HR045, HR050). The color contour depicts the meridional flow velocity, defined by $v_m = [\bar{v}_r^2 + \bar{v}_\theta^2]^{1/2}$ normalized by v_{rms} of each model. The streamlines are overplotted with a length proportional to the flow speed. The white dashed line denotes the interface between convection and radiative zones.

In order to reveal a cause of the difference in the critical value of the convective Rossby number between the two models, we present, in Figure 5, the dependence of the mean convective velocity (v_{rms}) on the convective Rossby number for the MHD (blue crosses) and HD (red diamonds) models. Here the regime around the transition is focused. When comparing two models at the same Ro_{conv} , the MHD model has the smaller convective velocity than the HD model. The MHD model thus can maintain the solar-type DR even at the lower rotation rate (thus higher convective Rossby number) in comparison with the HD model. Since the Lorentz force of the dynamo-generated magnetic field puts the brakes on the convective motion (e.g., Cattaneo et al. 2003; Brun et al. 2004), the MHD model becomes more rotationally-constrained than the HD model. This could be the reason why the magnetic field helps to produce the solar-type DR. Fan & Fang (2014) and Karak et al. (2014) also argued that the reduction of the convective velocity by the dynamo-generated magnetic field is responsible for the difference of the critical rotation rate (i.e., critical convective Rossby number) for the solar to anti-solar transition between the HD and MHD models. It is interesting that such a drastic difference between the MHD and HD models observed in v_{rms} (Fig.5) is unified in the view of the Ro-dependence (Fig.4b).

3.3. Bistability of the Rotation Profile

The transition between the solar and anti-solar type rotation patterns has been known since Gilman (1977) and studied in various settings (Käpylä et al. 2011; Gastine et al. 2013; Guerrero et al. 2013). However, the bistability of the rotation profile has not been sufficiently-studied because it has only recently been discovered (Gastine et al. 2014; Käpylä et al. 2014). We revisit here the dependence of the rotation profile on the history both in the MHD and HD models by taking either a solar-type (Set S: Runs MS and HS) and an anti-solar type (Set A: Runs MA and HA) solution as initial conditions.

In the Set S, we perform simulations by starting from the saturated state of MR040 (HR050) with the solar-type DR for the MHD (HD) run and decrease the rotation rate. In contrast, in the Set A, we choose the final state of MR025 (HR030) with the anti-solar type DR as the progenitor for the MHD (HD) model and increase the rotation rate. The DR parameter (α_e) for these models are shown in Figure 6(a) as a function of the convective Rossby number (Ro_{conv}). The models MS, MA, HS and HA are denoted by cyan triangles, green circles, pink crosses and orange squares, respectively. The DR parameters of the basic runs (MR and HR) are also shown by blue crosses and red diamonds as references.

As shown in Gastine et al. (2014) and Käpylä et al. (2014), the bistability of the rotation profile can be observed near the transition in the HD model. In the Set HS, the transition of the HD solution occurs when $0.58 < \text{Ro}_{\text{conv}} < 0.67$ while it does when $0.47 < \text{Ro}_{\text{conv}} < 0.52$ in the Set HA. On the other hand, the set MS started from the solar-type DR reproduces the similar results with the set MR with the initial rigid rotation (see cyan triangles and blue crosses). This is consistent with the recent studies of Fan & Fang (2014) and Karak et al. (2014) who found in their convective dynamo simulations that the bistability is disappeared and the DR profile becomes independent from the hysteresis when allowing the growth of the MHD dynamo. However, in the set MA which is started from the anti-solar type DR, the bistability seems to be not disappeared (see green circles).

The remaining of the bistability in the set MA of our MHD

models may be related to the presence of the stable layer underlying the convective envelope, which is a difference between our simulation model and the models adopted in Fan & Fang (2014) and Karak et al. (2014). Carefully studying the rotation profile of the MR030 (Fig.2a) which has a very similar rotation profile with the progenitor for the set MA, we can find that the stable layer has a strong equatorial acceleration despite the anti-solar type DR established in the convection zone. Since the differential rotation in the stable layer should change the latitudinal temperature and entropy distributions to achieve the thermal wind balance there (e.g., Kitchatinov & Rüdiger 1995; Rempel 2005), it may enforce the anti-solar type DR even in the high Ω_0 regime which should provide the solar-type DRs. Our speculation on the role of the stable layer in the maintenance of the internal rotation will be quantitatively examined in a subsequent paper.

It is interesting that, by using the Rossby number (Ro), we can again unify the transition between the solar and anti-solar type rotation profiles independently of the hysteresis. Shown in Figure 6(b) is the DR parameters of all the models as a function of the Rossby number. The symbols have the same meanings as those in Figure 6(a). It is found that the transition occurs at $\text{Ro} \simeq 1$ in all the simulation sets. Not only the critical value, the sharpness of the transition is also similar between all the cases. This confirms that the transition between the two rotation regimes is better captured by the Rossby number rather than by the convective Rossby number.

One important finding in our study is that the initial rotation profile, i.e., the evolution history of the stellar rotation, has an impact on the convective velocity if we does not allow the growth of the magnetic field. The dependence of the mean convective velocity (v_{rms}) on the convective Rossby number (Ro_{conv}) is shown in Figure 7. The symbols have the same meanings as those in Figure 6(a). Here the regime around the transition is focused. The bistable nature of the convective velocity can be seen in the HD models, while the MHD models have similar convective velocity around the transition. Thus, in the HD cases, the Set S (Set A) with the initial solar-type (anti-solar type) DR becomes more rotationally-dominated (inertia dominated) than the other sets. In contrast, in the MHD cases, the evolution history of the DR does not change the convective velocity and the rotational dominance in the system. This would be due to the regulation of the convective velocity by the dynamo-generated magnetic field. These indicate that the bistability appeared in the rotation profile is essentially a consequence of the hysteresis of the convective velocity, which can be weakened by the dynamo-generated magnetic field.

Since the convective Rossby number denotes the relative importance of the buoyancy force in comparison with the Coriolis force, the magnetic effect and the evolution history are not directly reflected in its definition. In contrast, the Rossby number describes the significance of the inertia force arising as the results of the hysteresis and the non-linear interaction between the convective motion and the magnetic field, relative to the Coriolis force. Therefore, the effects of the magnetic field and the hysteresis are naturally reflected in it. This would be the reason why the transition between the solar and anti-solar type rotation profiles can be unified in the view of the Ro-dependence.

3.4. Dependence of Magnetic Dynamo Activity on Rotation Rate

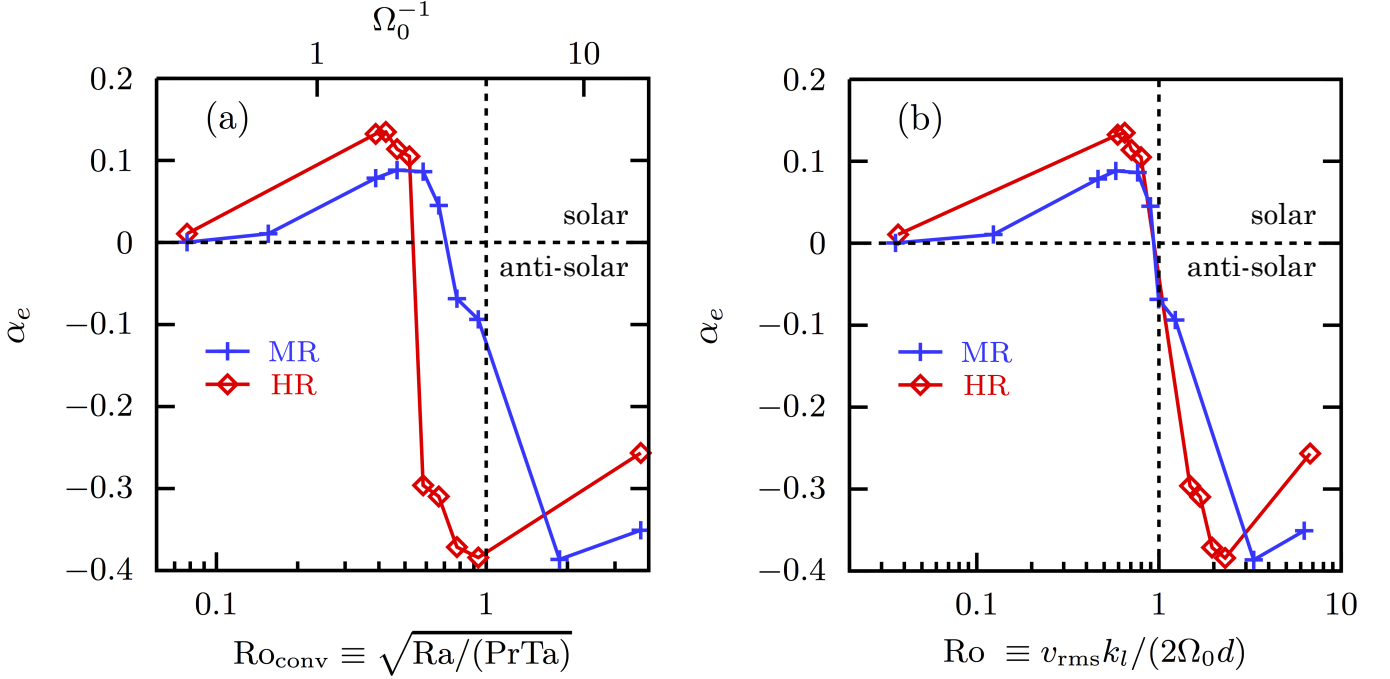


FIG. 4.— (a) DR parameter α_e as functions of the convective Rossby number (Ro_{conv}) and the corresponding rotation rate (Ω_0). The horizontal and vertical dashed lines indicate $\alpha_e = 0$ and $Ro_{\text{conv}} = 1$. (b) DR parameter α_e as a function of the Rossby number (Ro). The horizontal and vertical dashed lines indicate $\alpha_e = 0$ and $Ro = 1$. The blue crosses and red diamonds denote the MHD and HD models with the initial rigid rotation in both panels.

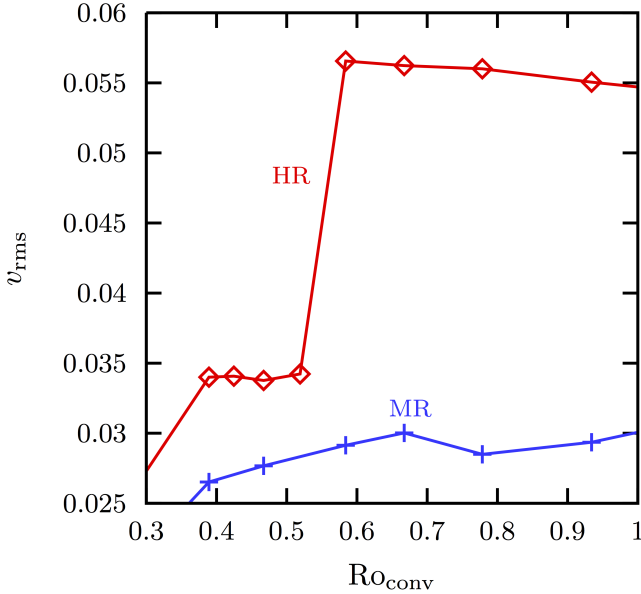


FIG. 5.— Mean convective velocity v_{rms} as a function of the convective Rossby number (Ro_{conv}). The blue crosses and red diamonds denote the MHD and HD models with the initial rigid rotation.

The MHD model exhibits a rich variety of the magnetic dynamo activity depending on the rotation rate. We show the time-latitude diagram of (a) $\langle B_r \rangle_\phi$ (left column), (b) $\langle B_\theta \rangle_\phi$ (middle column) and (c) $\langle B_\phi \rangle_\phi$ (right column) of MR00625, 025, 030, 050, 060, and 150 at $r = 0.65R$ (mid-stable zone) in Figure 8 and at $r = 0.85R$ (mid-convective zone) in Figure 9. Here the angular brackets with subscript ϕ denote the azimuthal average at a given depth. The time and amplitude are normalized by τ_c and B_{eq} , respectively. The red and blue tones denote the positive and negative mean-field strength. The hor-

izontal dashed-line in each panel denotes the equator. The upper three models have the anti-solar type DR and the lower three models are characterized by the solar-type DR. MR025–060 are the models near the transition.

The model with the smallest rotation rate is dominated by the turbulent magnetic field and has little large-scale component both in the radiative and convective layers (see MR00625). This would be due to the weak Coriolis force, yielding weak differential rotation. At around the transition of the rotation profile, the spatiotemporal coherence of the magnetic field becomes remarkable. In the slow rotation regime with the anti-solar type DR, a quasi-steady large-scale magnetic field with a dipole symmetry is organized (see MR025 and 030). $\langle B_r \rangle_\phi$ and $\langle B_\theta \rangle_\phi$ are stronger in the convection zone rather than in the radiative zone, while $\langle B_\phi \rangle_\phi$ is stronger in the stable zone than in the convection zone. Among the three magnetic components, $\langle B_\phi \rangle_\phi$ is dominant in these models. The large-scale B_ϕ -component is the strongest at the mid-latitude and is antisymmetric about the equator. This is consistent with the shearing of the B_θ -component, i.e., Ω -process, by the anti-solar type DR.

The properties of the magnetic dynamo change drastically across the transition of the DR profile. The large-scale magnetic field shows the polarity reversal in the fast rotation regime with the solar-type DR. In the models near the transition, i.e., MR050 and 060, the large-scale magnetic component with polarity reversals is built up mainly in the stable zone. It has commonly B_ϕ -dominance. The large-scale B_ϕ -component is the strongest at around the equator in these models unlike the models with the anti-solar type DR in which it is the strongest at the mid-latitude. In MR050, the convection zone is dominated by the turbulent magnetic field. However, we can observe a weak spatiotemporal coherence of the magnetic field in the convection zone in MR060. It is interesting that the cycle of the polarity reversal of the large-scale mag-

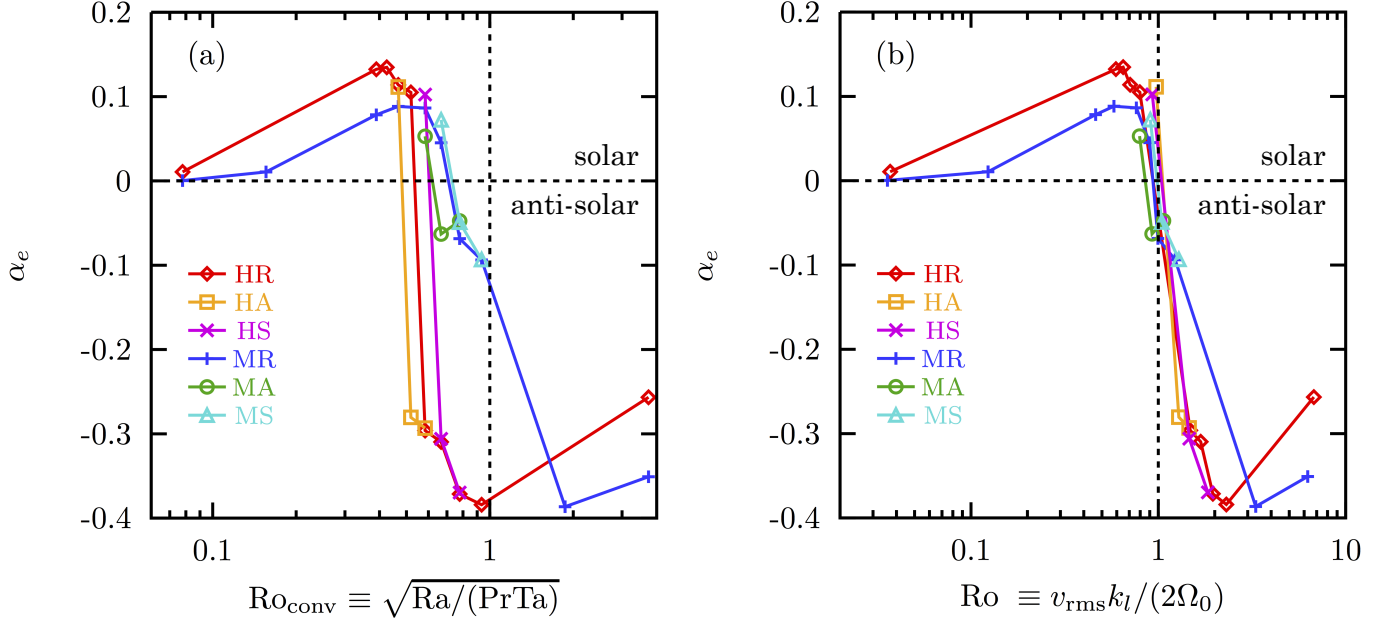


FIG. 6.— DR parameters (α_e) of the models with non-rigid initial rotations as functions of (a) the convective Rossby number (Ro_{conv}) and (b) the Rossby number (Ro). The models MS, MA, HS and HA are denoted by cyan triangles, green circles, pink crosses and orange squares, respectively in both panels. The horizontal and vertical dashed lines indicate (a) $\alpha_e = 0$ & $Ro_{\text{conv}} = 1$ and (b) $\alpha_e = 0$ and $Ro = 1$. The DR parameters of the basic runs (MR and HR) are shown by blue crosses and red diamonds as references.

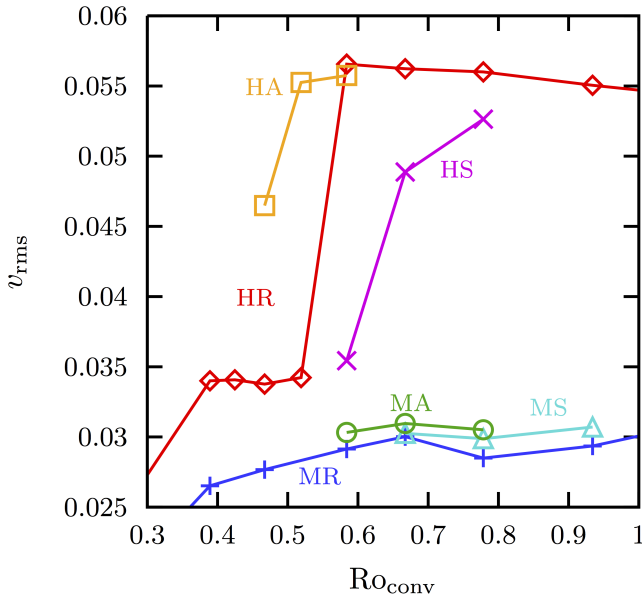


FIG. 7.— Mean convective velocity v_{rms} as a function of the convective Rossby number (Ro_{conv}). The models MR, MS, MA, HR, HS and HA are denoted by blue crosses, cyan triangles, green circles, red diamonds, pink crosses and orange squares, respectively.

netic field around the equator is shorter in the convection zone than in the radiative zone.

The most intriguing dynamo activity can be observed in the model with a fast rotation beyond the transition (see MR150). Note that this model has 3–4 times higher rotation rate than that adopted in the model around the transition. In the stable zone, the strong large-scale magnetic component with a dipole symmetry is built up. It concentrates at the high latitudinal region ($\simeq 80^\circ$) and seems to have a long cycle period of the polarity reversal ($\tau_{\text{cyc}} \gtrsim 200\tau_c$). The spatial distribution of

the B_ϕ -field suggests that the Ω -effect plays a crucial role in amplifying the large-scale magnetic field in the stable region. In the convective envelope, two types of the dynamo mode can be clearly observed. The long-lasting magnetic component with a dipole symmetry, which is similar to that in the stable zone, is found in the high latitude. In contrast, at around the equatorial region, the oscillatory dynamo mode with a shorter cycle period ($\tau_{\text{cyc}} \simeq 10\tau_c$) and a poleward migration is excited and sustained. The difference of the dynamo mechanism between the models with the different rotation profiles is discussed in §4.

4. DISCUSSION: THE RELATION BETWEEN MAGNETIC DYNAMO ACTIVITY AND KINETIC HELICITY

The purpose of this paper is to elucidate the effect of the magnetic field on the formation of the rotation profile. Nevertheless, a rich variety of the magnetic dynamo activity observed in the MHD models (see §3.4) makes us interested in their dynamo mechanisms. Here we discuss a possible key ingredient for the oscillatory magnetic dynamo with focusing on its relation to the kinetic helicity of the convection flow.

As an indicator of the magnetic dynamo activity, we study the relative amplitude of the magnetic energy to the kinetic energy which is measured by the ratio ϵ_M/ϵ_K , where ϵ_M and ϵ_K are mean magnetic and kinetic energy densities at the saturated state (see §3 for the definitions of ϵ_M and ϵ_K). In addition, the mean kinetic helicity (net helicity), \mathcal{H}_{ave} , of each MHD model is also evaluated, where it is defined by

$$\mathcal{H}_{\text{ave}} = (|\mathcal{H}_N| + |\mathcal{H}_S|)/2, \quad (9)$$

with

$$\mathcal{H}_i \equiv \langle v \cdot (\nabla \times v) \rangle_i \quad (i = N, S). \quad (10)$$

Here the angular brackets with subscripts ‘‘N’’ and ‘‘S’’ denote the time- and volume-average in the northern and southern hemispheric convection zones at the saturated state.

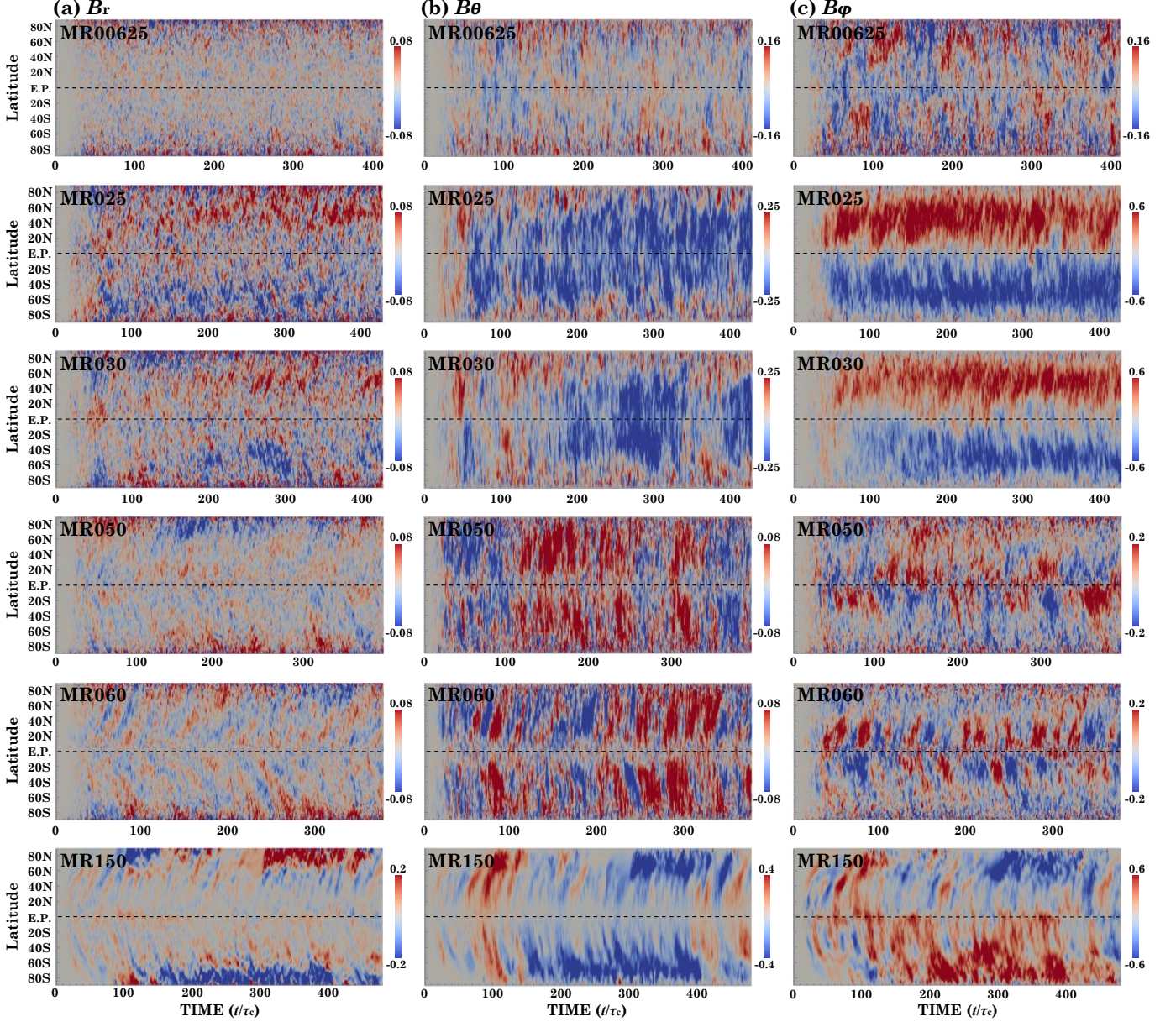


FIG. 8.— Time-latitude diagram of (a) $\langle B_r \rangle_\phi$ (left column), (b) $\langle B_\theta \rangle_\phi$ (middle column) and (c) $\langle B_\phi \rangle_\phi$ (right column) at $r = 0.65R$ (mid-stable zone) for the models MR00625, 025, 030, 050, 060, and 150, respectively. The time and the amplitude are normalized by τ_c and B_{eq} . The red and blue tones denote the positive and negative mean-field strength. Horizontal black dashed-line corresponds to the equator. The top three models have the anti-solar type DR and the bottom three models have the solar-type DR.

Shown in Figure 10 is ϵ_M/ϵ_K (blue line with diamonds [right axis]) and \mathcal{H}_{ave} (red line with circles [left axis]) as a function of the Rossby number (Ro) for the basic MHD runs (Set MR). The vertical dashed line denotes $\text{Ro} = 1$. The ratio ϵ_M/ϵ_K has a bit complicated profile: In the regime of the small or large Rossby number, that is $\text{Ro} \ll 1$ or $\text{Ro} \gg 1$, ϵ_M/ϵ_K decreases with the increase of Ro . In contrast, at around the transition, the higher Ro rather provides the larger ϵ_M/ϵ_K .

The mean kinetic helicity shows a single peak profile with the maximum at around $\text{Ro} \simeq 1$ where the transition from the solar to anti-solar type rotation profiles occurs. In the regime of $\text{Ro} \lesssim 1$ where the solar-type DR is established, ϵ_M/ϵ_K anticorrelates with \mathcal{H}_{ave} . By contrast, the ratio decreases with the kinetic helicity in the anti-solar type rotation regime of $\text{Ro} \gtrsim 1$. Since the temporal property of the large-scale magnetic

field also changes from the oscillatory to the stationary across $\text{Ro} \simeq 1$ as was described in §3.4, this suggests that the dynamo mechanism would be associated in some way with the kinetic helicity in the convection zone.

The Ro -dependence of the net kinetic helicity, which shows a peak at moderate rotation rate, is deeply related to the formation of the convective column. Since the angular velocity is lower in the regime of the anti-solar type DR or $\text{Ro} \gg 1$, the up-down asymmetry of the convective motion is lower, leading to less preference for one sign of the kinetic helicity. On the other hand, in the regime of the solar-type DR or $\text{Ro} \ll 1$, the convection has a tendency to align in columnar rolls parallel to the rotation axis (see §3.1). In the convection columns, the velocity is mostly perpendicular to the rotation axis while the vorticity is mostly parallel to the rotation axis,

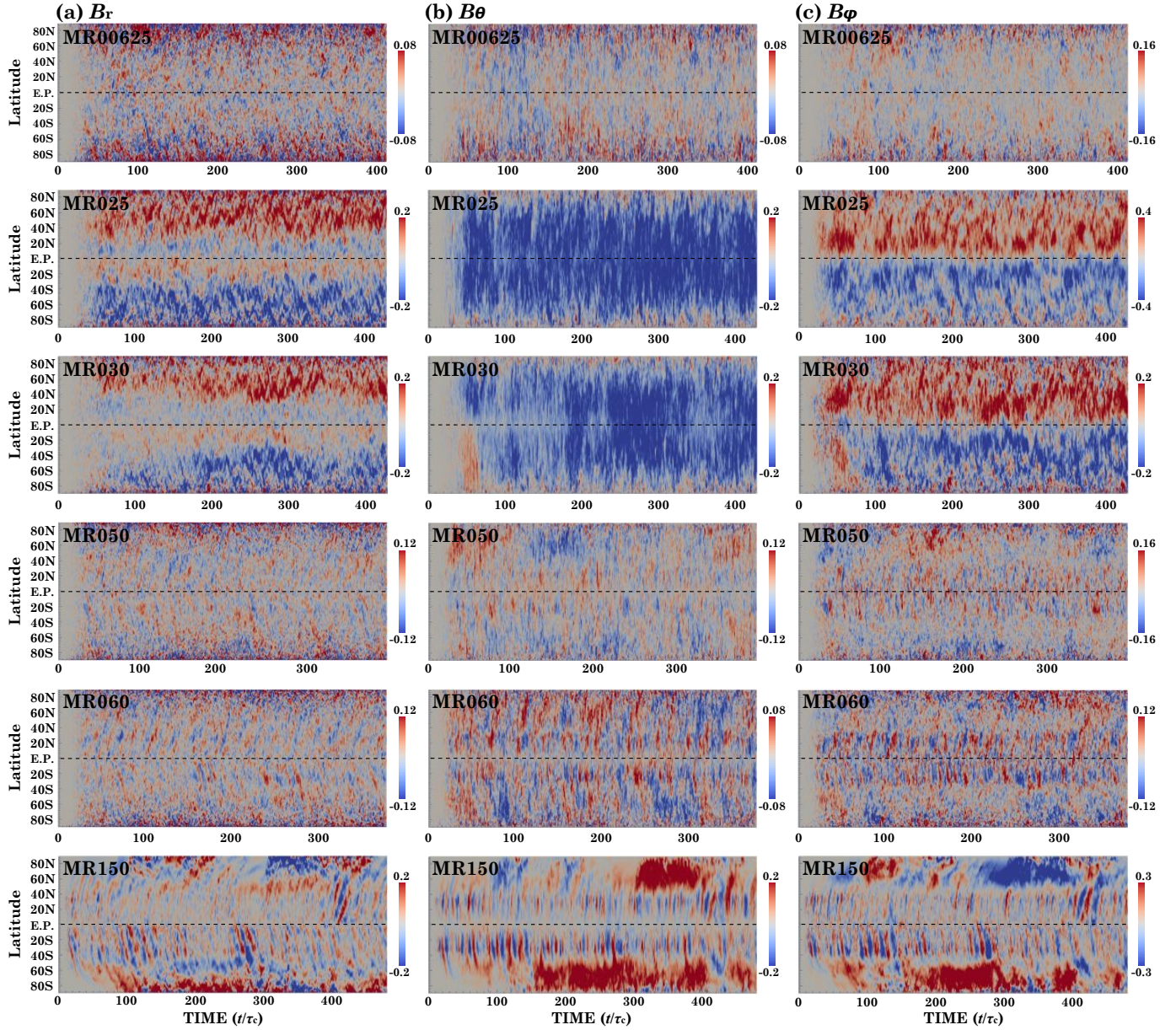


FIG. 9.— Same as Figure 8 but at $r = 0.85R$ (mid-convection zone).

resulting in a small net kinetic helicity (e.g., Knobloch et al. 1981; Browning 2008). It was also clearly demonstrated by Sprague et al. (2006) with asymptotic numerical analysis of unstratified turbulence that the largest net kinetic helicity is established at moderate rotation rate and decreases as rotation becomes even more rapid (see also, Käpylä et al. 2009).

The anti-correlation between Ro and ϵ_M/ϵ_K in the solar-type DR regime would be consistent with the earlier studies (e.g., Brown et al. 2011; Käpylä et al. 2013). In addition, the correlation between Ro and ϵ_M/ϵ_K around the transition is also compatible with the numerical result of Karak et al. (2014) (see their Table 2). However, the role of the kinetic helicity in the magnetic dynamo mechanism and its hidden connection to the observed relationship between stellar rotation and magnetic activity (e.g., see Güdel 2007; Reiners 2012, for reviews) remain to be fully elucidated although there are a great deal of work exploring the linkage between them (e.g.,

Knobloch et al. 1981; Jennings & Weiss 1991; Baliunas et al. 1996; Brandenburg et al. 1998, 2012).

To get a better grasp of the relation of the kinetic helicity and the magnetic dynamo mechanism, in Figure 11, we show the distribution of the time and azimuthally-averaged kinetic helicity, $\overline{\mathcal{H}}(r, \theta) \equiv \overline{v \cdot (\nabla \times v)}$, for the models MR00625, 025, 030, 050, 060, and 150, respectively. The red and blue tones denote the positive and negative helicity. The horizontal black dotted-line corresponds to the equator. The dashed curve denotes the interface between the convection and radiative zones. The models listed in the upper three panels have the anti-solar type DR (MR00625, 025 and 030) and the lower three panels correspond to the models with the solar-type DR (MR050, 060 and 150). To clearly demonstrate the latitudinal distribution of the kinetic helicity, the radial average of the time- and azimuthally-averaged kinetic helicity, i.e., $\langle \overline{\mathcal{H}} \rangle_r \equiv \langle v \cdot (\nabla \times v) \rangle_r$, is also shown in Figure 12, where

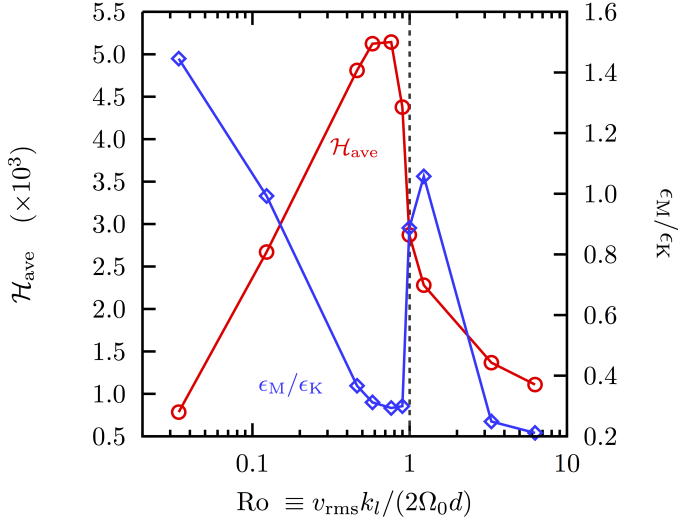


FIG. 10.— Mean helicity defined by $\mathcal{H}_{ave} \equiv (|\mathcal{H}_N| + |\mathcal{H}_S|)/2$ (red circles) and ratio ϵ_M/ϵ_K (blue diamonds) as a function of the Rossby number (Ro) for the basic MHD runs.

angular brackets with subscript r denote the radial average. The different line-types denote the models with different Ω_0 .

It would be trivial that the kinetic helicity has an antisymmetric profile with respect to the equator in the model with a sufficiently fast rotation. In the northern (southern) hemisphere, the negative (positive) helicity becomes predominant. This is because the downflow with the negative (positive) helicity is on average stronger than the upflow with the positive (negative) helicity in the northern (southern) hemisphere in the density stratified system (e.g., Spruit et al. 1990; Miesch 2005). The weaker equatorial antisymmetry of the kinetic helicity profile in the model with the smallest rotation (MR00625) would be a result of a weaker Coriolis force which provides less impact on the convective motion. The peak amplitude of the kinetic helicity is little dependent on the rotation rate (within factor 2). However, we can find from Figure 12 that the latitude for the peak of the kinetic helicity decreases as the rotation rate increases: While the higher latitudinal region has a larger helicity in the models with the anti-solar type DR (MR00625, 025, and 030), the lower latitudinal region has a larger helicity in the models with the solar-type DR (MR050, 060, and 150).

It is the most remarkable that both the hemispheric and inter-hemispheric latitudinal gradients of the kinetic helicity become larger around the equator with the increase of the rotation rate. In the models with the solar-type DR and the oscillatory large-scale magnetic field, the kinetic helicity concentrates on around the equatorial plane and has strong hemispheric and inter-hemispheric latitudinal gradients there. In contrast, the models with the anti-solar type DR and the stationary large-scale magnetic field do not show the significant latitudinal gradient of the kinetic helicity around the equatorial region. Since, when comparing Figures 9 and 11, the latitude providing the stronger large-scale magnetic field overlaps with that with the larger kinetic helicity, it is expected that the latitudinal distribution of the kinetic helicity is a key to distinguish the dynamo mechanisms. The larger the latitudinal gradient of the kinetic helicity around the equator becomes, the more the oscillatory large-scale magnetic field would be developed.

Recently, Mitra et al. (2010) reported an intriguing find-

ing in their dynamo simulation by a forced helical turbulence in a wedge-shaped spherical shell that the oscillatory large-scale magnetic field with equatorial migration can be organized, even without the Ω -effect, essentially due to an inter-hemispheric gradient of the kinetic helicity. They argued that the α^2 -dynamo mode excited by the helical turbulence with the equatorial antisymmetry is responsible for the oscillatory property. Furthermore, a connection between α^2 -dynamo mode and solar magnetism was discussed in some recent results of convective MHD dynamos simulations (e.g., Simard et al. 2013; Masada & Sano 2014a,b).

When considering the latitudinal gradient of the kinetic helicity around the equator as an important ingredient of the oscillatory property of the dynamo even in our simulations, we can speculate the reason why there exists a difference of the dynamo property depending on the regime of the rotation profile. Since the model with the smaller rotation rate and thus the anti-solar type DR does not have a sufficient latitudinal gradient of the kinetic helicity around the equator to excite the oscillatory α^2 -dynamo mode, the Ω -effect solely works to build up the large-scale magnetic field and thus yields a stationary solution. In contrast, the model with the faster rotation and thus the solar-type DR has a sufficient concentration and strong latitudinal gradient of the kinetic helicity around the equator, yielding the oscillatory large-scale magnetic component sustained by the α^2 -effect in addition to the Ω -effect.

The detailed analysis with mode expansion by Legendre polynomials on kinetic helicity and magnetic field will be presented in a subsequent paper in which we focus on the magnetic dynamo activity and its dependences on the rotation rate and stratification level. Although a quantitative description of the dynamo mechanism is beyond the scope of this paper, we can speculate from our simulation results that accurate numerical modeling of the kinetic helicity profile in the actual solar interior will offer a way to unveil the mystery of the solar magnetism.

5. SUMMARY

In this paper, the effect of the magnetic field on the mean DR profile established in the convection zone was systematically studied by comparing the MHD and HD models of the rotating spherical shell convection in the broad range of the initial rotation rate. A fully compressible Yin-Yang MHD code which was developed in MYK13 and a stellar model consisting of the convection zone and the radiative zone were used for the simulation. The critical parameter which controls the transition between the anti-solar type and solar-type DR profiles was explored with focusing on the ‘‘Rossby number (Ro)’’ and the ‘‘convective Rossby number (Ro_{conv})’’. In addition, the bistability of the rotation profile, which has only recently been discovered by Gastine et al. (2014), was revisited under the influence of the magnetic field. Our main findings are summarized as follows.

1. The critical value of the Ro_{conv} for the transition was higher in the MHD model than the HD model. The transition was more gradual in the model under the influence of the magnetic field. Comparing two models at the same Ro_{conv} , the magnitude of the DR parameter (α_e) was smaller in the MHD model than in the HD model. The magnetic field had a crucial role in suppressing the DR and facilitated to produce the solar-type rotation profile. Since the Lorentz force of the dynamo-generated magnetic field reduced the convective velocity, the MHD model became more rotationally-constrained

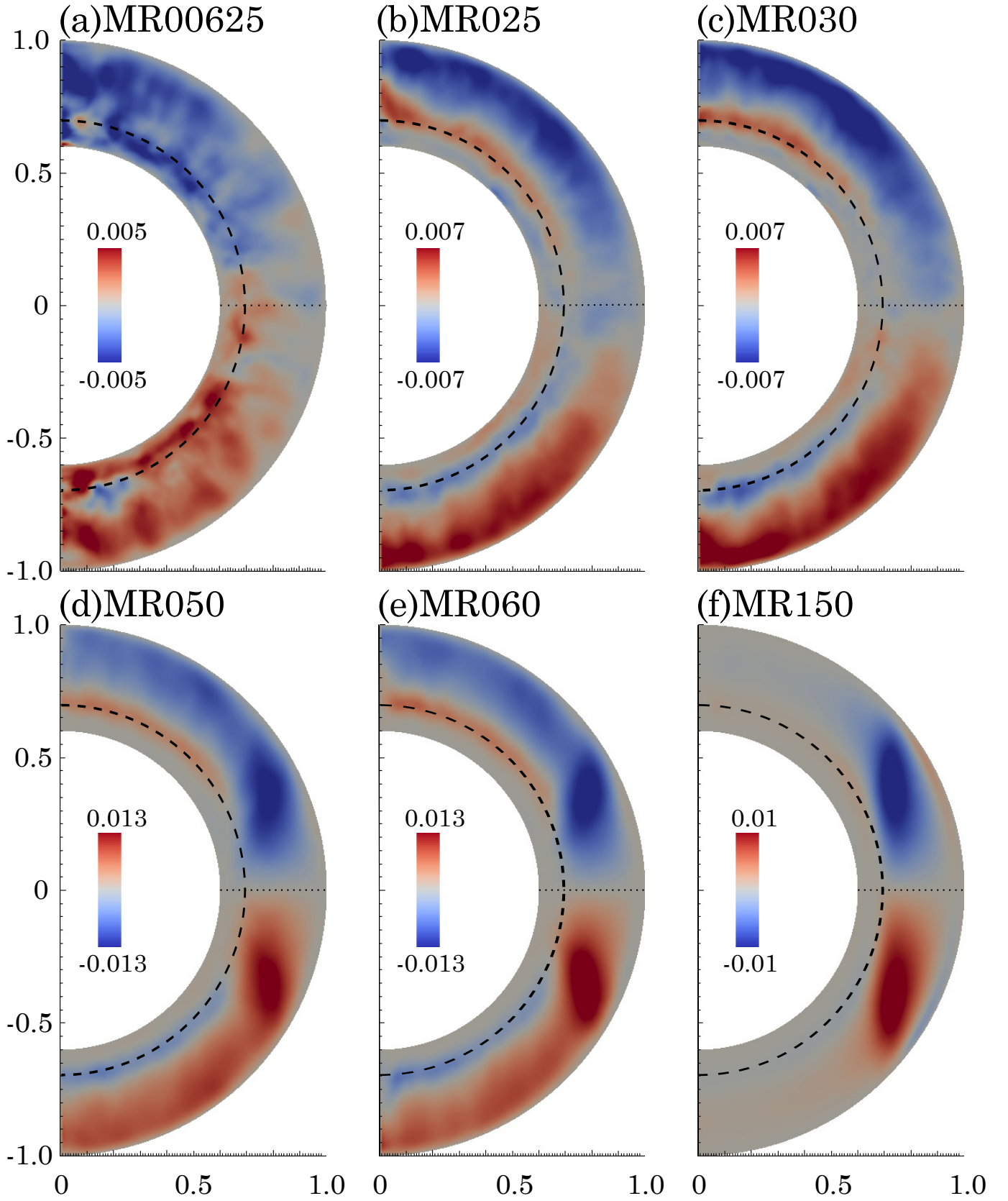


FIG. 11.— Time and azimuthally-averaged kinetic helicity $\overline{\mathcal{H}}(r, \theta)$ for the models MR00625, 025, 030, 050, 060, and 150, respectively. The red and blue tones denote the positive and negative helicity. The black dotted-line corresponds to the equator. The dashed curve denotes the interface between the convection and radiative zones. The upper three models have the anti-solar type DR and the lower three models have the solar-type DR.

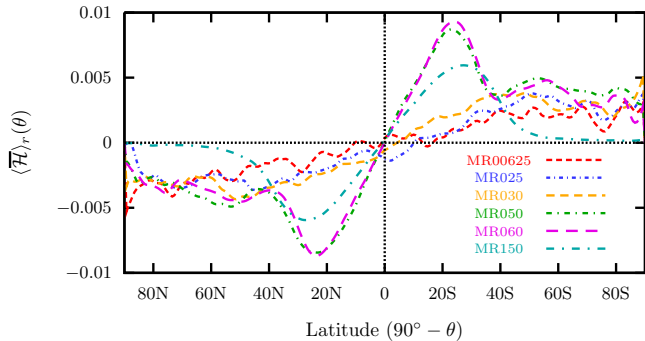


FIG. 12.— Latitudinal distribution of the averaged kinetic helicity, i.e., $\langle \overline{\mathcal{H}} \rangle_r \equiv \langle \overline{v \cdot (\nabla \times v)} \rangle_r$. The different line types denote the models with different Ω_0 .

than the HD model. This would be the reason why the magnetic field facilitated to produce the solar-type DR.

2. The transition from the solar to anti-solar type rotation profiles occurred at $Ro \simeq 1.0$ both in the MHD and HD models. Not only the critical value, the sharpness of the transition was also similar between the two models in the view of Ro -dependence. The solar-type DR, accompanied by the columnar convection and multi-cell meridional circulation pattern, was established in the regime $Ro \lesssim 1$. The anti-solar type DR, characterized by the cellular convections and the single-cell meridional circulation, developed in the regime of $Ro \gtrsim 1$ regardless of the presence of the magnetic field. The transition between the two rotation profiles was controlled by the Ro rather than by the Ro_{conv} .

3. From the point of view of the Ro_{conv} -dependence, the rotation profile showed, as was observed in earlier studies, the bistability near the transition in the HD model while it disappeared when allowing the growth of the dynamo-generated magnetic fields except for the model with taking an anti-solar type solution as the initial condition. It was found that the transition between the anti-solar and solar-type DR profiles could be unified in the view of Ro -dependence independently of the hysteresis. The transition between the two rotation regimes was again better captured by the Ro rather than by the Ro_{conv} .

4. The influence of the magnetic field or the history on the convective velocity would be responsible for the dependence of the rotation profile on it. Such effects were not reflected in the Ro_{conv} by definition. In contrast, it could be definitely captured by the Ro . The transition between the solar and anti-solar type rotation profiles was thus unified in the view of the Ro -dependence.

5. A rich variety of the magnetic dynamo activity could be observed in the MHD models. In the regime of the anti-solar type DR ($Ro \gtrsim 1$), the stationary large-scale magnetic

field with a dipole symmetry was built up both in the stable and convection layers except for the model with the smallest rotation rate. In contrast, the oscillatory large-scale magnetic component was organized in the model with the solar-type DR profile ($Ro \lesssim 1$). The latitudinal profile of the kinetic helicity would be a key to distinguish the dynamo mechanisms between the two rotation regimes. The oscillatory large-scale magnetic field could be organized when the strong latitudinal gradient of the kinetic helicity existed around the equator.

Our parametric study was conducted by the simulation model with the same value of the Rayleigh number. The supercriticality level $\delta \equiv [Ra - Ra_c]/Ra_c$, which is an essential measure of the turbulence level, was thus not constant and varied with the rotation rate as shown in Table 1 (see the third column). In order to compare the models with the supercriticality level fixed, we should change the Ekman number or Prandtl number, or density stratification, providing a possible difference in the resultant flow pattern.

Gastine et al. (2013,2014) indicated that, while the transition between the solar and anti-solar type rotation DR profiles would take place at almost the same Ro_{conv} independently of the density stratification and Ekman number, the lower Ekman number or the stronger density stratification would produce the steeper transition. It was also suggested that the higher Prandtl number would shift the critical Ro_{conv} to the higher value at least in the high Ekman number regime. Not only on the flow properties, these parameters would also have an influence on the magnetic dynamo activities (c.f., Käpylä et al. 2011, 2014; Karak et al. 2014). To verify the universality of the critical Rossby number for the transition obtained in this study, further parameter study is indispensable and is planned as our future work.

The recent development of the astroseismology opens up the way to study the large-scale internal flows in the solar-type main sequence stars with different age and thus different rotation rate (e.g., Chaplin et al. 2010). Computer simulation in tandem with the advanced observation will help deepening the understanding of the stellar interior dynamics and stellar dynamo activities in the astroseismology era.

We thank the anonymous referees for constructive comments. Numerical computations were carried out on Cray XC30 at Center for Computational Astrophysics, National Astronomical Observatory of Japan. This work was supported by JSPS KAKENHI grant Nos. 24740125 and 20260052.

REFERENCES

- Al-Shamali, F.M., Heimpel, M.H., & Aurnou, J.M. 2004, *Geophysical and Astrophysical Fluid Dynamics*, 98, 153
- Aurnou, J., Heimpel, M., & Wicht, J. 2007, *Icarus*, 190, 110
- Baliunas, S. L., Nesme-Ribes, E., Sokoloff, D., & Soon, W. H. 1996, *ApJ*, 460, 848
- Basu, S., & Antia, H.M. 2001, *MNRAS*, 324, 498
- Beaudoin, P., Charbonneau, P., Racine, E., & Smolarkiewicz, P.K. 2013, *Sol. Phys.*, 282, 335
- Brandenburg, A., Sokoloff, D., & Subramanian, K. 2012, *Space Sci. Rev.*, 169, 123
- Brandenburg, A., Saar, S. H., & Turpin, C. R. 1998, *ApJ*, 498, L51
- Brown, B. P., Miesch, M. S., Browning, M. K., Brun, A. S., & Toomre, J. 2011, *ApJ*, 731, 69
- Browning, M.K. 2008, *ApJ*, 676, 1262
- Brummell, N.H., Hurlburt, N.E., & Toomre, J. 1996, *ApJ*, 473, 494
- Brummell, N.H., Hurlburt, N.E., & Toomre, J. 1998, *ApJ*, 493, 955
- Brun, A.S., & Toomre, J. 2002, *ApJ*, 570, 865
- Brun, A.S., Miesch, M.S., & Toomre, J. 2004, *ApJ*, 614, 1073
- Busse, F.H. 1970, *Journal of Fluid Mechanics*, 44, 441
- Cattaneo, F., Emonet, T., & Weiss, N. 2003, *ApJ*, 588, 1183
- Charbonneau, P., Christensen-Dalsgaard, J., Henning, R., et al. 1999, *ApJ*, 527, 445
- Charbonneau, P. 2005, *Living Reviews in Solar Physics*, 2, 2

- Charbonneau, P. 2010, *Living Reviews in Solar Physics*, 7, 3
- Chan, K.L. 2010, *IAU Symposium*, 264, 219
- Chaplin, W.J., Appourchaux, T., Elsworth, Y., et al. 2010, *ApJ*, 713, L169
- Christensen, U.R., & Aubert, J. 2006, *Geophysical Journal International*, 166, 97
- Fan, Y., & Fang, F. 2014, *ApJ*, 789, 35
- Gastine, T., Wicht, J., & Aurnou, J.M. 2013, *Icarus*, 225, 156
- Gastine, T., Yadav, R.K., Morin, J., Reiners, A., & Wicht, J. 2014, *MNRAS*, 438, L76
- Giles, P.M., Duvall, T.L., Scherrer, P.H., & Bogart, R.S. 1997, *Nature*, 390, 52
- Gilman, P.A. 1977, *Geophysical and Astrophysical Fluid Dynamics*, 8, 93
- Glatzmaier, G.A., & Gilman, P.A. 1981, *ApJS*, 47, 103
- Glatzmaier, G.A., & Gilman, P. A. 1982, *ApJ*, 256, 316
- Gough, D.O., & McIntyre, M.E. 1998, *Nature*, 394, 755
- Güdel, M. 2007, *Living Reviews in Solar Physics*, 4, 3
- Guerrero, G., Smolarkiewicz, P.K., Kosovichev, A.G., & Mansour, N.N. 2013, *ApJ*, 779, 176
- Howe, R. 2009, *Living Reviews in Solar Physics*, 6, 1
- Jennings, R. L., & Weiss, N. O. 1991, *MNRAS*, 252, 249
- Kageyama, A., & Sato, T. 2004, *Geochemistry, Geophysics, Geosystems*, 5, 9005
- Käpylä, P. J., Korpi, M. J., & Brandenburg, A. 2009, *ApJ*, 697, 1153
- Käpylä, P.J., Mantere, M.J., & Brandenburg, A. 2011, *Astronomische Nachrichten*, 332, 883
- Käpylä, P. J., Mantere, M. J., Cole, E., Warnecke, J., & Brandenburg, A. 2013, *ApJ*, 778, 41
- Käpylä, P.J., Käpylä, M. J., & Brandenburg, A. 2014, *A&A*, 570, AA43
- Karak, B.B., Kapyla, P.J., Kapyla, M.J., & Brandenburg, A. 2014, *arXiv:1407.0984*
- Kitchatinov, L.L., & Ruediger, G. 1995, *A&A*, 299, 446
- Knobloch, E., Rosner, R., & Weiss, N. O. 1981, *MNRAS*, 197, 45P
- Komm, R.W., Howard, R.F., & Harvey, J.W. 1993, *Sol. Phys.*, 147, 207
- Kovári, Z., Bartus, J., Strassmeier, K.G., et al. 2007, *A&A*, 474, 165
- Kovari, Z., Kriskovics, L., Künstler, A., et al. 2014, *arXiv:1411.1774*
- Krause, F., Rüdiger, G. 1974, *Astronomische Nachrichten*, 295, 93
- Krause, F., & Raedler, K.-H. 1980, *Mean-field Magnetohydrodynamics and Dynamo Theory* (Oxford:Pergamon)
- Kitchatinov, L.L., & Ruediger, G. 1995, *A&A*, 299, 446
- Kosovichev, A.G., Schou, J., Scherrer, P.H., et al. 1997, *Sol. Phys.*, 170, 43
- Masada, Y. 2011, *MNRAS*, 411, L26
- Masada, Y., Yamada, K., & Kageyama, A. 2013, *ApJ*, 778, 11
- Masada, Y., & Sano, T. 2014, *PASJ*, 66, S2
- Masada, Y., & Sano, T. 2014, *ApJ*, 794, LL6
- Miesch, M.S., Elliott, J.R., Toomre, J., et al. 2000, *ApJ*, 532, 593
- Miesch, M. S. 2005, *Living Reviews in Solar Physics*, 2, 1
- Mitra, D., Tavakol, R., Käpylä, P.J., & Brandenburg, A. 2010, *ApJ*, 719, L1
- Moffatt, H.K. 1978, *Magnetic field generation in electrically conducting fluids*, Cambridge University Press
- Pedlosky, J. 1987, *Geophysical Fluid Dynamics*, by Joseph Pedlosky. Springer, New York. 1987
- Reiners, A. 2012, *Living Reviews in Solar Physics*, 9, 1
- Rempel, M. 2005, *ApJ*, 622, 1320
- Ruediger, G. 1989, *Differential rotation and stellar convection. Sun and the solar stars*, Berlin: Akademie Verlag, 1989
- Schou, J., Antia, H.M., Basu, S., et al. 1998, *ApJ*, 505, 390
- Schrinner, M., Petitdemange, L., & Dormy, E. 2012, *ApJ*, 752, 121
- Simard, C., Charbonneau, P., & Bouchat, A. 2013, *ApJ*, 768, 16
- Spiegel, E. A., & Zahn, J. P. 1992, *A&A*, 265, 106
- Sprague, M., Julien, K., Knobloch, E., & Werne, J. 2006, *Journal of Fluid Mechanics*, 551, 141
- Spruit, H. C., Nordlund, A., & Title, A. M. 1990, *ARA&A*, 28, 263
- Steffen, M., & Freytag, B. 2007, *Astronomische Nachrichten*, 328, 1054
- Strassmeier, K.G., Kratzwald, L., & Weber, M. 2003, *A&A*, 408, 1103
- Thompson, M.J., Christensen-Dalsgaard, J., Miesch, M.S., & Toomre, J. 2003, *ARA&A*, 41, 599
- Ulrich, R.K. 2010, *ApJ*, 725, 658
- Weber, M., Strassmeier, K.G., & Washuettl, A. 2005, *Astronomische Nachrichten*, 326, 287
- Zhao, J., Bogart, R.S., Kosovichev, A.G., Duvall, T.L., Jr., & Hartlep, T. 2013, *ApJ*, 774, LL29